JGR Space Physics

RESEARCH ARTICLE
10.1029/2024JA032672

Spatial Features of the Delayed Ionospheric Response During Low and High Solar Activity

Erik Schmölter[1], Hanna Dühnen[1], Jens Berdermann[1], Rajesh Vaishnav[2], and Christoph Jacobi[2]

[1]German Aerospace Center, Institute for Solar-Terrestrial Physics, Neustrelitz, Germany, [2]University Leipzig, Leipzig Institute for Meteorology, Leipzig, Germany

Key Points:

- The global delayed ionospheric response to solar EUV increases with the solar activity level
- Latitude- and longitude-dependent changes of the delayed ionospheric response are observed between low and high solar activity
- The delayed ionospheric response varies significantly for selected EUV bands

Correspondence to:

E. Schmölter,
Erik.Schmoelter@dlr.de

Citation:

Schmölter, E., Dühnen, H., Berdermann, J., Vaishnav, R., & Jacobi, C. (2024). Spatial features of the delayed ionospheric response during low and high solar activity. *Journal of Geophysical Research: Space Physics*, *129*, e2024JA032672. https://doi.org/10.1029/2024JA032672

Received 20 MAR 2024
Accepted 4 MAY 2024

Abstract The ionospheric response to solar 27-day signatures has complex temporal and spatial variations, which are driven by short- and long-term changes of the solar activity among other processes (e.g., geomagnetic activity). A delay between these solar and ionospheric signatures occurs due to accumulation of plasma, which depends on the rates of photoionization, photodissociation and recombination in the upper atmosphere. The balance of these processes changes significantly at different solar activity levels. Therefore the present study investigates the delayed ionospheric response during low and high solar activity. For that purpose, global as well as latitude- and longitude-dependent total electron content (TEC) is analyzed via superposed epoch analysis (SEA). Different results based on the solar proxy F10.7 and solar extreme ultraviolet (EUV) irradiance measurements are presented to discuss findings of preceding studies and to provide a first wavelength-dependent analysis of the spatial features. The SEA shows a good correlation between solar activity level and delayed ionospheric response with particular strong enhancements of the delay at mid-latitudes. Increased delays are also observed for morning and evening hours. Thus, the present study confirms the correlation of delayed ionospheric response and solar activity level as indicated in preceding studies, and also quantifies the temporal and spatial variations with commonly used data sets. This in turn allows a better understanding of the processes that cause the delayed ionospheric response.

1. Introduction

The delayed ionospheric response describes the peak time difference or cross-correlation lag of solar and ionospheric 27-day signatures, which are commonly represented by wavelength-dependent solar extreme ultraviolet (EUV) flux and height-dependent (or integrated) electron density. The delay between these signatures occurs through accumulation processes that cause a maximum in electron density after the maximum in solar activity. This is controlled in particular by the rates of ionization and recombination (Ren et al., 2018; Schmölter et al., 2022), but dissociation (Jakowski et al., 1991; Schmölter & von Savigny, 2022; Schmölter et al., 2022) and transport processes (Vaishnav, Jacobi, et al., 2021; Vaishnav, Schmölter, et al., 2021) have significant impact, too. In the first phase of the 27-day solar rotation period, production and loss of O^+ in the upper ionosphere increase due to the rise of solar activity. This process is enhanced when more O is produced in the lower ionosphere by photodissociation of O_2 and transported upward (Schmölter & von Savigny, 2022; Schmölter et al., 2022). In the second phase of the 27-day solar rotation period, production and also loss of O^+ in the upper ionosphere decrease due to the drop of solar activity. The dominating recombination processes within this phase are not immediate, leading to accumulation and an observed time difference between the solar and ionospheric 27-day signature (Schmölter & von Savigny, 2022; Schmölter et al., 2022).

The delayed ionospheric response has spatial and seasonal variations, depending on different thermospheric and ionospheric processes, but can also change with other periodic solar variations (e.g., the 11-year solar cycle) and geomagnetic activity (Schmölter, Berdermann, Jacobi, & Jakowski, 2020; Schmölter, Berdermann, Jakowski, & Jacobi, 2020; Vaishnav, Jacobi, et al., 2021; Vaishnav, Schmölter, et al., 2021). Various preceding studies conclude that the delayed ionospheric response increases with increasing solar activity, but this relationship has not yet been quantified. The relationship with geomagnetic activity, however, is complex, and previous studies show that various conditions (such as season, latitude, or phase of the 11-year solar cycle) influence the impact on the delayed ionospheric response (Schmölter, Berdermann, Jakowski, & Jacobi, 2020; Vaishnav et al., 2019). The present study is a first approach to quantify the relation of the delayed ionospheric response to solar radiation changes.

The 11-year solar cycle, which is observed with the number of sunspots and the corresponding solar flux changes, introduces solar activity levels for the solar 27-day signatures (average flux during each rotation). These changes significantly influence the global ionosphere (Vaishnav et al., 2019), and their impact on the delayed ionospheric response was indicated, for example, for the ascending phase of solar cycle 24 (Schmölter, Berdermann, Jakowski, & Jacobi, 2020). The present study extends these results and investigates the delayed ionospheric response for the whole solar cycle 24 to calculate solar activity level dependent values. Specifically, the range from 80 to 180 sfu for the solar proxy F10.7 and the range from 10^{-6} to 10^{-3} $W{\cdot}m^{-2}$ nm^{-1} for wavelength-dependent solar EUV is investigated (mean values of 27-day solar rotation period).

The superposed epoch analysis (SEA) method (also known as composite analysis) was successfully used to extract significant signatures from different solar, ionospheric and thermospheric measurement data (Schmölter & von Savigny, 2022; Schmölter et al., 2022). The same method is applied in the present study, but the approach is extended with solar activity level, geomagnetic activity level, latitude, longitude and local time. This addition to the earlier approach allows to extract the delay for each parameter in order to investigate a possible correlation.

The SEA method is applied to F10.7 and total electron content (TEC) as well as the global mean TEC (GTEC) to discuss the peak time difference and cross-correlation lag based on the 27-day signatures. The spatial changes and the correlation with solar activity are estimated. These results are of particular interest as preceding modeling studies of the delayed ionospheric response used F10.7 driven solar flux models (Ren et al., 2018; Schmölter et al., 2022; Vaishnav et al., 2018, 2019, 2023; Vaishnav, Jacobi, et al., 2021; Vaishnav, Schmölter, et al., 2021). The SEA method is further applied to F10.7 and wavelength-dependent solar EUV irradiance to confirm wavelength-dependent delays between the data as reported by Schmölter and von Savigny (2022). These results are used to discuss the limitations of solar proxies for analysis of the delayed ionospheric response. A comprehensive overview of spatial, solar activity and local time driven variability of the delayed ionospheric response is provided. Geomagnetic activity is also briefly discussed to show that its impact is successfully removed via the SEA method.

2. Data

The present study uses the SEA method, which was successfully applied in preceding studies to investigate processes driving the delayed ionospheric response (Schmölter & von Savigny, 2022; Schmölter et al., 2022).

Generally, measurement data are presented at a temporal resolution of 1 day in figures to emphasize the 27-day solar rotation period. The SEA method is applied to the measurement data at original temporal resolution. Cross-correlations, on the other hand, are applied to averaged or interpolated measurement data at temporal resolution of 1 hr calculated via linear interpolation. This approach has been successfully used in preceding studies to combine data of different temporal resolution. Cross-correlations may be affected to some extent if interpolation is applied, but relative changes of the lag are presented accurately.

Calculations are performed in geographic coordinates, but the World Magnetic Model (NCEI Geomagnetic Modeling Team & British Geological Survey, 2019) is used to add, for example, the inclination into the maps. This adequately represents the influence of Earth's magnetic field.

2.1. Solar Radio Flux and Kp Index

The general solar activity is described with the 10.7 cm solar radio flux (F10.7) that is commonly used as solar proxy for the solar EUV flux (Tapping, 2013). The geomagnetic activity, which affects the ionospheric state as well (Field & Rishbeth, 1997), is described with the planetary Kp index that measures the disturbances of the horizontal component of Earth's magnetic field (Matzka, Stolle, et al., 2021). Both, F10.7 and Kp, were applied in various studies of the delayed ionospheric response and good correlations were reported (Schmölter, Berdermann, Jakowski, & Jacobi, 2020; Vaishnav, Schmölter, et al., 2021). F10.7 measurements are provided by the National Research Council (NRC) Canada (NRC, 2023) and Kp measurements are provided by the German Research Center for Geosciences (GFZ) Potsdam (GFZ, 2023; Matzka, Bronkalla, et al., 2021). Both data sets are also included in the National Aeronautics and Space Administration (NASA) Goddard Space Flight Center's (GSFC) OMNI database, that can be accessed through the OMNIWeb interface (NASA, 2023).

2.2. Solar Spectral EUV Irradiance

The Extreme ultraviolet Variability Experiment (EVE) of the Solar Dynamics Observatory (SDO) missions measures the solar irradiance (Didkovsky et al., 2009; Hock et al., 2010; Pesnell et al., 2011; Woods et al., 2010) with two Multiple EUV Grating Spectrographs (MEGS) from 6 to 17 nm (A), from 17 to 37 nm (A) and from 37 to 106 nm (B). These measurements are combined to a merged spectrum including all wavelengths from 5.8 to 106.2 nm at 0.02 nm sampling. The full spectra are available from 30 April 2010 to 26 May 2014. After that, the spectra are only measured from 33.34 to 106.2 nm, as no data is available for shorter wavelengths due to the malfunction of the MEGS-A (on 26 May 2014). This period is sufficient for the SEA method though, since several studies (Schmölter, Berdermann, Jakowski, & Jacobi, 2020; Schmölter et al., 2018; Vaishnav, Schmölter, et al., 2021) applied these data to reliably calculate the delayed ionospheric response to solar 27-day signatures. For that reason, the present study applies the level 2 data (version 7) with temporal resolution of 10 s, which are provided by the University of Colorado Boulder (CU) Laboratory for Atmospheric and Space Physics (LASP) via the EVE home page (LASP, 2023).

2.3. Total Electron Content Maps

TEC, an integral measurement for the ionospheric electron density, is provided as global maps by the International Global Navigation Satellite System (GNSS) Service (IGS) (Hernández-Pajares et al., 2009). Several data centers provide different products which are used to calculate IGS combined maps. TEC maps were applied in several studies of the delayed ionospheric response and were in good agreement with results using other thermospheric and ionospheric parameters (Schmölter, Berdermann, Jakowski, & Jacobi, 2020; Schmölter et al., 2021). Thus, TEC is an appropriate parameter to describe the general state of the ionosphere in the present study. The high-rate TEC maps (one map per hour) are provided via the IGS home page (IGS, 2023).

3. Superposed Epoch Analysis of F10.7 and TEC

The SEA method is applied to detect and average 27-day signatures for solar and ionospheric parameters (Schmölter & von Savigny, 2022; Schmölter et al., 2022). For this purpose, F10.7 anomaly time series are calculated by subtracting a 35-day running mean from the original F10.7 time series. The calculated F10.7 anomaly time series is further filtered with a 5-day running mean to remove high frequency oscillations (e.g., day-to-day variability). The 27-day solar rotation periods (epochs) are defined by the respective local maxima of the resulting time series and are applied in the further analysis. As suggested by Schmölter et al. (2022), only those epochs are considered which are characterized by significant anomalies greater than 7.5 sfu. The F10.7 and global mean TEC (GTEC, mean of all grid points) time series as well as the F10.7 anomaly time series are shown in Figure 1. Epoch centers are marked with black dots in Figure 1b.

The averaged signatures for the original and anomaly time series for F10.7 and GTEC are shown in Figures 2a and 2c. Preceding studies applied peak time difference $dt_{\max}$ and cross-correlation lag τ according to the first row of Figure 2 for the comparison of different measurement data (Schmölter et al., 2021, 2022). Other studies applied both parameters according to the second row of Figure 2 for the comparison with modeling results (Schmölter et al., 2022). The present study describes the delay with the cross-correlation lag of the original time series (Figure 2b) where for quiet conditions (all epochs) a global mean delay of 26 hr is estimated.

The significance of the SEA results is calculated with the Monte-Carlo method applied by preceding studies (Schmölter et al., 2022; Schmölter & von Savigny, 2022). This test repeats the SEA method for 1,000 random selections and calculates a 27-day sinusoidal fit for each result (gray lines in Figure 2c). The fraction of these fits with an amplitude greater than the amplitude of the epoch averaged GTEC anomaly describes the significance. This fraction approaches 0% for the results in Figure 2 as only significant anomalies are considered. Additionally, the fraction is even smaller than values reported by Schmölter and von Savigny (2022) for height-dependent electron density. The better result is due to GTEC following solar activity more strongly and both, height-dependent and local processes, having a smaller impact.

The presented SEA method using 1-dimensional time series can be extended to data sets with more dimensions after the epochs are identified. Wavelength- and height dependent delays were calculated in preceding studies (Schmölter et al., 2022), but the present study includes latitude, longitude and local time instead and thus provides insight into spatial variability. For example, extending the analysis applied for Figure 2b to longitude- and

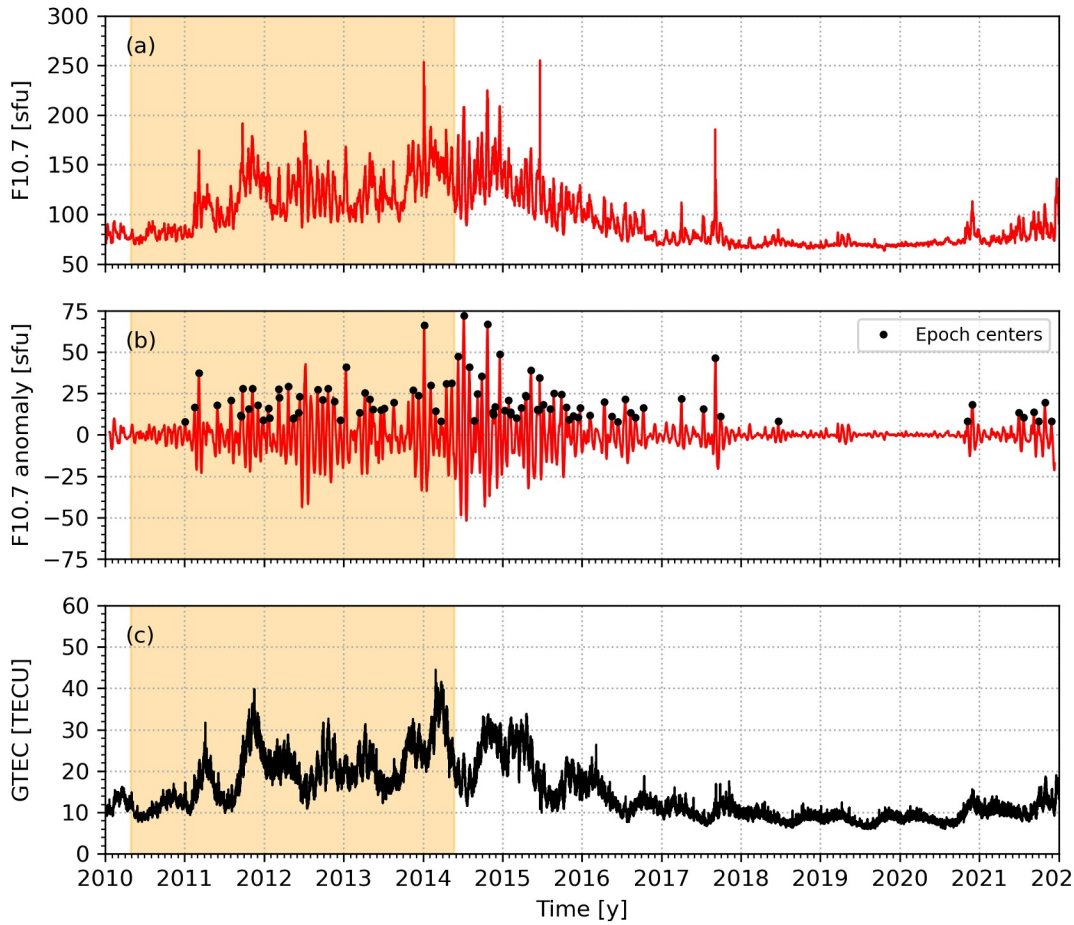

Figure 1. F10.7 (a), F10.7 anomaly with epoch centers (b) and GTEC (c) from 2010 to 2022. The orange shading indicates the period with EUV spectra from 5.8 to 106.2 nm.

latitude-dependent TEC allows to calculate the map in Figure 3 (analysis at each grid point). Several features of delay discussed in preceding studies are reflected with these estimated delays. The hemispheric asymmetry (Vaishnav et al., 2019), increases toward mid-latitudes (Schmölter, Berdermann, Jakowski, & Jacobi, 2020), enhancements at the equatorial ionization anomaly crests (Ren et al., 2018) are confirmed. Thus, the approach is appropriate to identify further features of the delayed ionospheric response.

4. Solar Flux Driven Delay Variability Analyzed via F10.7

The impact of solar activity is calculated by categorizing all epochs (see Figure 1b) according to the maximum F10.7 (window of 27 d). A sufficient amount of samples (minimum of 10, mean of 20) for each category is required and therefore an overlap (7.5 sfu) for increments of 2.5 sfu is applied. For each increment, the SEA method is applied and the peak time difference as well as the cross-correlation lag are estimated. The results of this analysis are shown in Figure 4. The peak time differences (magenta dots) are not well correlated with F10.7 levels, since there are small variations in the 27-day signatures (see Figure 1a), which may weaken the correlation (correlation coefficient of 0.48). For example, any secondary peak may cause significant changes of the delay. The cross-correlation lag is less susceptible to such small variations and a clear correlation (correlation coefficient of 0.72) with F10.7 levels occurs. However, a linear correlation between both parameters seems to occur only in the range from 120 to approximately 160 sfu. Below 120 sfu and from 160 to 180 sfu, no significant delay changes are observed. Thus, a polynomial fit (third order) appears more appropriate to describe these variation (black dashed line in Figure 4). This approach reduces the root mean square error (RMSE) of 6.97 hr for the linear

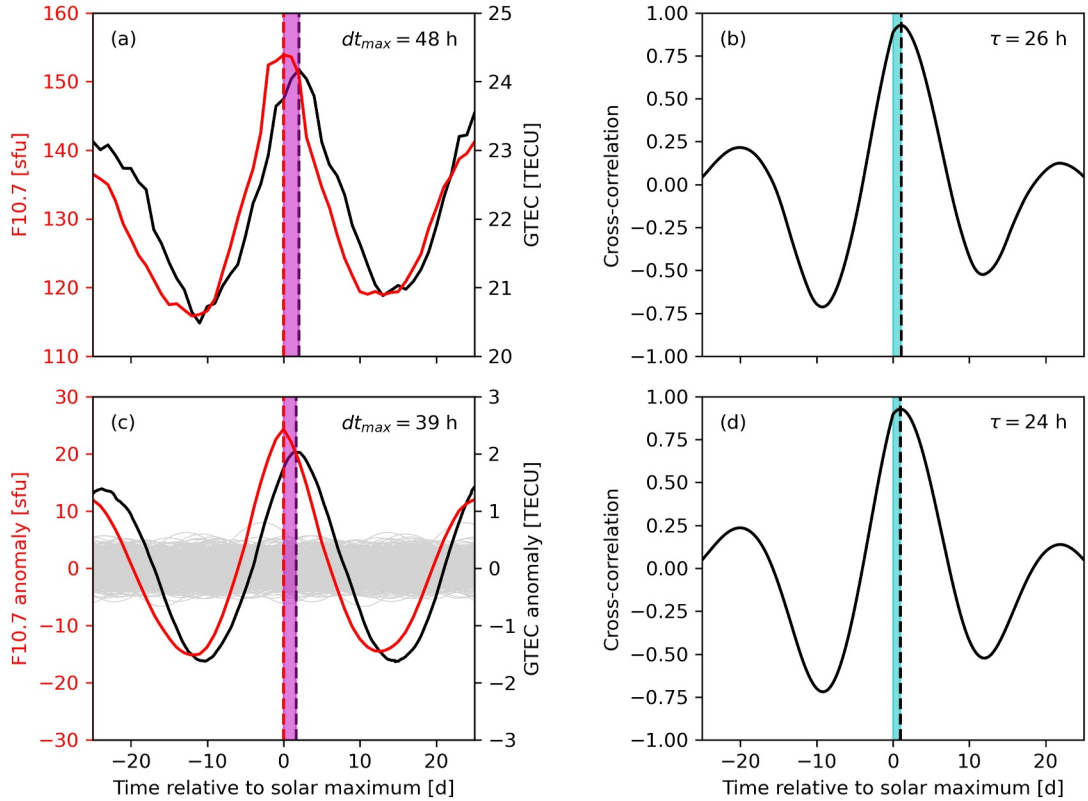

Figure 2. F10.7 and GTEC signatures (a), F10.7 and GTEC anomaly signatures (c) as well as corresponding cross-correlations (b, d) are shown. The peak time difference and cross-correlation lag are marked with the magenta and cyan shading. The gray lines in (c) are a sample result of the Monte-Carlo significance test.

approximation to 6.29 hr for the polynomial approximation (correlation coefficient of 0.85). Both solutions show an increase of approximately 0.88 hr/sfu in the range from 120 to 160 sfu.

The correlation of the delayed GTEC response with the solar activity level does not describe spatial variations and is therefore not appropriate for studies with interest in local ionospheric changes. For that reasons, delay maps as in Figure 3 are calculated for solar activity from 120 to 140 sfu and 140 to 160 sfu. Both maps and the corresponding latitude-dependent means are shown in Figure 5. Increased delays are observed for higher solar activity, but particularly prominent are the changes of the spatial distribution, which results in different latitude-dependent mean variations as well.

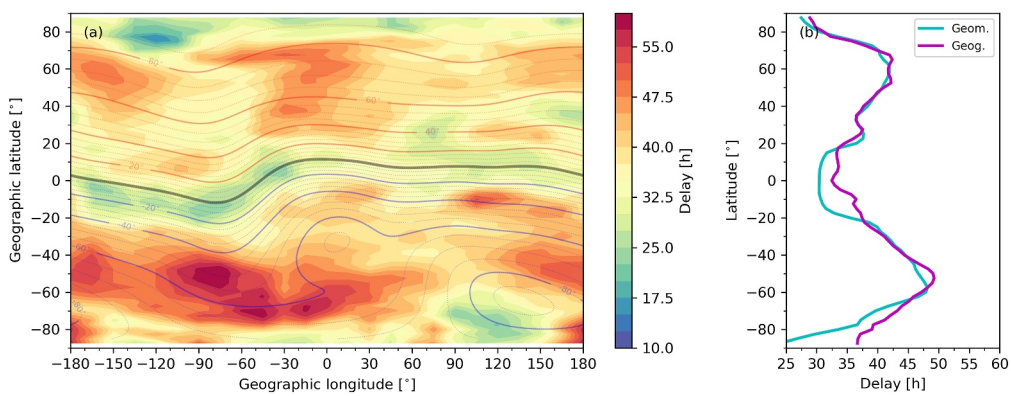

Figure 3. Cross-correlation lag (delay) via the SEA method for all epochs and World Magnetic Model (WMM) inclination (red and blue lines) are shown (a). The latitude-dependent mean is given for geographic and geomagnetic latitude (b).

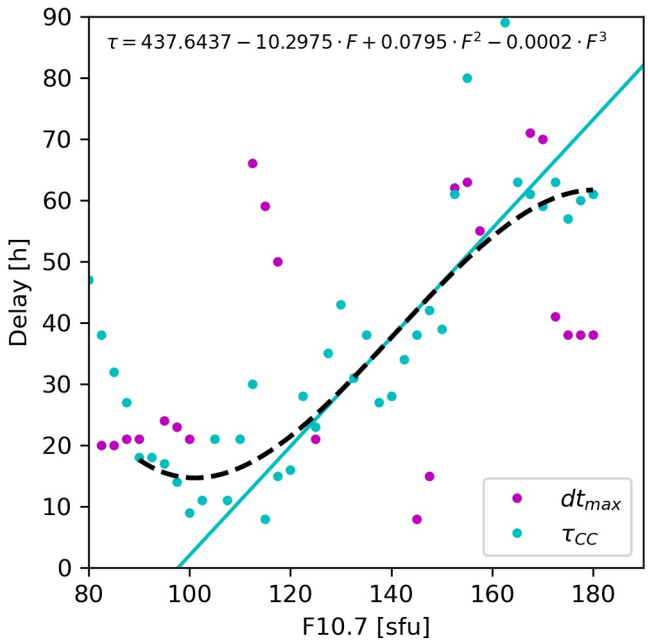

Figure 4. Scatter plot of F10.7 and delay (peak time difference dt_{max} and cross-correlation lag τ_{CC}). The linear regression (solid cyan line) and a polynomial approximation of the third order (dashed black line) for the cross-correlation lag are shown (coefficients rounded to 4 digits).

The map for lower solar activity (see Figure 5a) has enhancements of the delay along the equatorial ionization anomaly crests, at mid-latitudes in the South American sector and at mid-latitudes in the European sector. The strongest delay increases occur in the equatorial ionization anomaly crests and decreases toward the Equator and mid-latitudes are observed. These variations agree with latitude-dependent analyses by Ren et al. (2018) and Schmölter, Berdermann, Jakowski, and Jacobi (2020). Both studies investigated the delayed ionospheric response in periods (2003 and from 2011 to 2013) that have mean solar activity (128.4 and 118.67 sfu) similar to the range applied in Figure 5a. Strong deviations occur at high-latitudes (and negative delays), which may be related to the stronger impact of geomagnetic activity and different processes that control the ionospheric state in this region (Hunsucker & Hargreaves, 2007). The map for higher solar activity (see Figure 5c) has enhancements of the delay along the equatorial ionization anomaly crests as well as Southern hemisphere high-latitudes. The most noticeable feature is the hemispheric asymmetry (increase in the Southern hemisphere), which agrees with latitude-dependent results of analyses by Vaishnav, Schmölter, et al. (2021).

Figure 6 presents the differences of Figures 5a and 5c, thus showing the spatial variations in more detail. The strongest increases of the delay with F10.7 are observed in mid- and high-latitudes, which in turn indicates an increase in the accumulation (ionization and dissociation). Other processes may contribute to these changes (especially at high-latitudes), but could only be investigated with data in higher spatial resolution. Decreases of the delay are observed at approximately 20°N and 20°S, which do not follow the geomagnetic equator. Thus, the changes in the equatorial ionization anomaly crests (see Figure 5) may be superposed with further processes, that are less responsive to the ionospheric plasma flow, for example, thermospheric transport processes (Lei et al., 2011) or coupling with the lower atmosphere.

The observed changes of the delayed ionospheric response are generally in good agreement with preceding studies, but the range of delays (from 0 to 3 d) is greater than values reported by investigations of specific 27-day solar rotation periods. The height-dependent analysis via the SEA method by Schmölter and von Savigny (2022) also identified delays of more than 2 d. Additionally, these delays are only observed during high solar activity when a strong accumulation is expected.

5. Superposed Epoch Analysis of Wavelength-Dependent EUV Irradiance and TEC

Schmölter and von Savigny (2022) investigated height- and wavelength-dependent changes of the delayed ionospheric response via the SEA method and applied epoch centers calculated from F10.7 anomalies to solar spectral irradiance measured by the Solar EUV Experiment (SEE) of the Thermosphere Ionosphere Mesosphere Energetics and Dynamics (TIMED) mission. This analysis showed different delays with F10.7 and solar EUV dependent on wavelength, which are crucial to consider when comparing studies based on either data set. Thus, the results in Figures 2–6 are appropriate for comparison with preceding studies based on F10.7 (Schmölter et al., 2022), but may differ significantly compared to studies based on solar EUV (Schmölter et al., 2018). For that reason, the SEA method is further applied to describe changes between F10.7 and solar EUV in more detail, but also to describe the temporal and spatial features of the delayed ionospheric response based on wavelength-dependent 27-day signatures.

The epoch centers in Figure 1b are applied to wavelength-dependent solar EUV irradiance measured by SDO/EVE and for each time series the 27-day signatures and corresponding delays are calculated with the same process as presented with GTEC (see Figure 2). The results in Figure 7 confirm the findings by Schmölter and von Savigny (2022) and wavelength-dependent delays are observed. The gray lines in Figure 7a show the solar EUV irradiance signatures at each wavelength with different deviations. The mean signature (black line) shows a delay of approximately 1 d and a lower minimum during the second phase of the 27-day period. These two features were also observed with solar EUV irradiance measured by TIMED/SEE (Schmölter & von Savigny, 2022). Figure 7b

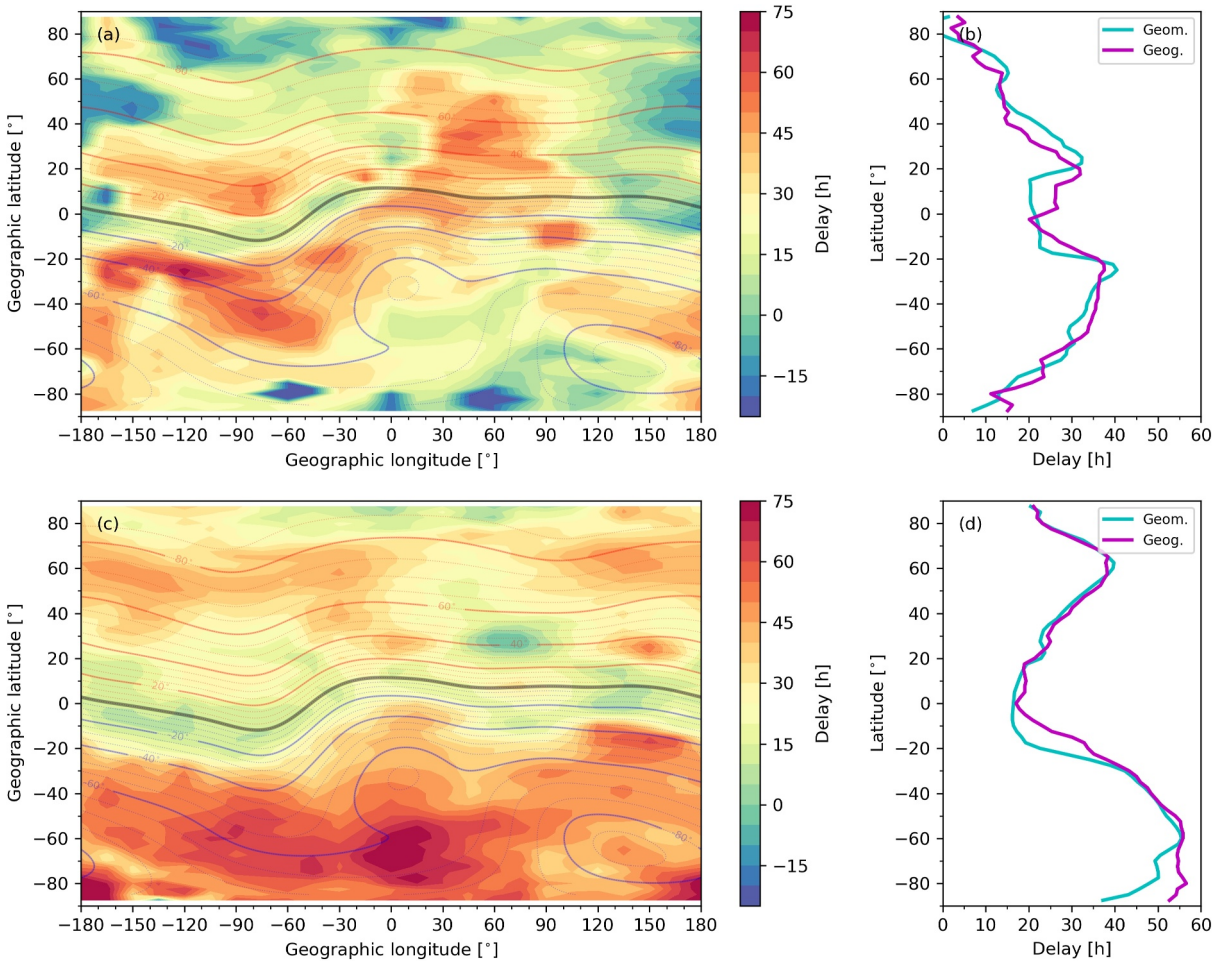

Figure 5. Cross-correlation lag (delay) via the SEA method for epochs with solar activity from 120 to 140 sfu (a) and 140 to 160 sfu (c) as well as World Magnetic Model (WMM) inclination (red and blue lines) are shown. The corresponding latitude-dependent means are given for geographic and geomagnetic latitudes (b, d).

shows the wavelength-dependent signatures in more detail. A significant difference is observed for signatures at wavelengths shorter and longer than approximately 33 nm. There are also significantly less correlated signatures around this wavelength. These features are due to the different data periods available for either wavelength range, which is due to the malfunction of MEGS-A on 26 May 2014.

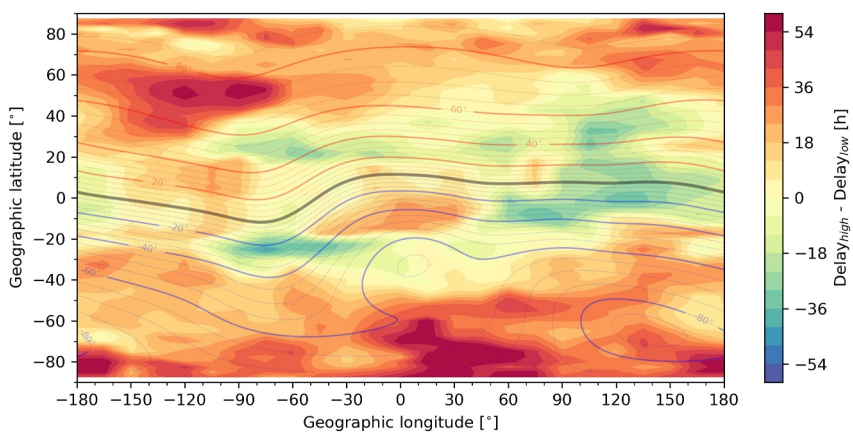

Figure 6. Difference of cross-correlation lag (delay) via the SEA method for epochs with solar activity from 120 to 140 sfu and 140 to 160 sfu as well as World Magnetic Model (WMM) inclination (red and blue lines) are shown.

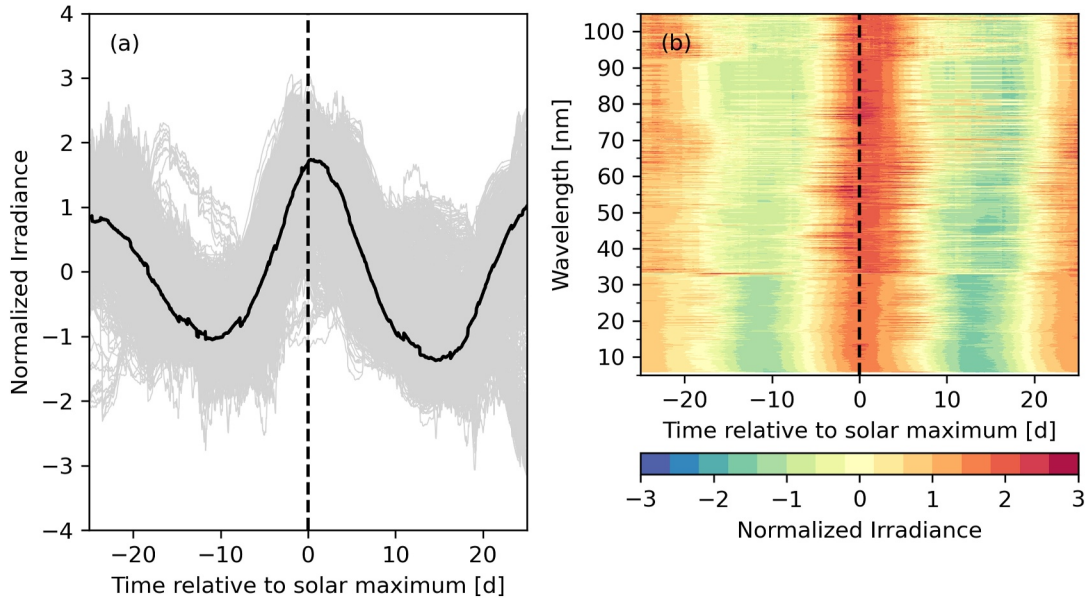

Figure 7. Solar EUV irradiance signatures (a) at different wavelengths (gray lines) and the mean of these signatures (black line) are shown. The wavelength-dependent signatures are shown in more detail in the heatmap (b). The standard score is applied to normalize the signatures. The solar maximum of the 27-day signatures is centered according to F10.7 epoch centers.

Figure 8 shows the wavelength-dependent peak time difference and cross-correlation lag of F10.7 and solar EUV irradiance signatures. The peak time differences according to bins of 1 nm (black line in Figure 8a) is less than 25 hr at wavelengths shorter than 30 nm and increases up to 50 hr at wavelengths from 30 to 40 nm, from 60 to 70 nm and from 90 to 105 nm. The distribution of the peak differences (magenta dots) is continuous, but outliers in clusters at increments of approximately 1 d occur for less correlated signatures due the applied interpolation. The distribution of the cross-correlation lags (cyan dots) is not affected by this as the approach is less susceptible to deviations. The cross-correlation lag (black line in Figure 8b) has a qualitatively similar variability to the peak time differences at wavelengths shorter than 60 nm and longer than 90 nm. A strong increase up to 100 hr is observed at wavelengths from 60 to 90 nm with a mean of approximately 50 hr. The differences that occur are important for the understanding of the delayed ionospheric response, since different absorption processes in the upper atmosphere occur dependent on the wavelength (Fennelly & Torr, 1992). An increase of the delay at longer

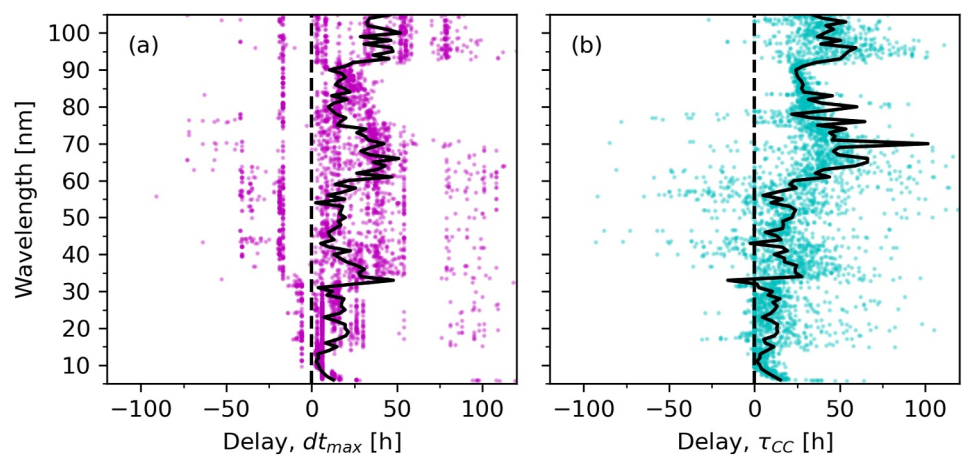

Figure 8. Wavelength-dependent peak time difference (a) and cross-correlation lag (b) of F10.7 and solar EUV irradiance signatures are shown with the colored dots. The black lines show mean values for bins of 1 nm.

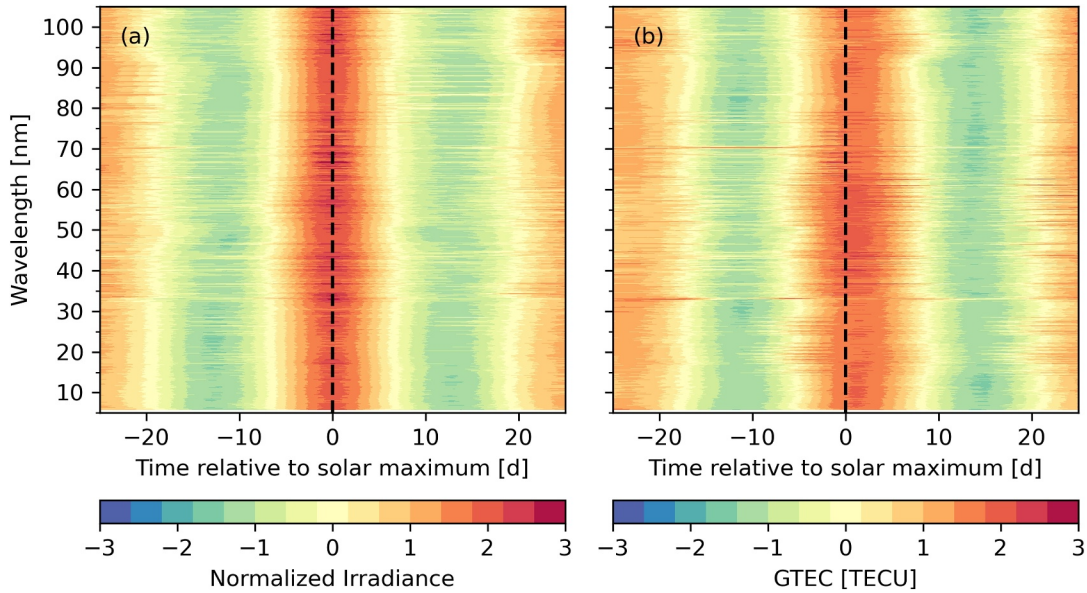

Figure 9. The wavelength-dependent irradiance (a) and GTEC (b) signatures are shown in the heatmaps (a, b). The standard score is applied to normalize the solar irradiance signatures. The solar maximum of the 27-day signatures is centered according to solar irradiance epoch centers. These epoch centers differ dependent on wavelength.

wavelengths affects the photodissociation of O_2 in the lower ionosphere (Schmölter & von Savigny, 2022) and may cause changes that do not correlate with variations of F10.7.

Schmölter and von Savigny (2022) investigated the height- and wavelength-dependent variability in more detail with the 27-day signatures based on the epoch centers calculated from F10.7 anomalies. This provided relative delays between solar and ionospheric parameters. An analysis independent of F10.7 is also of interest and the subsequent analysis is based on epoch centers that are calculated separately at each wavelength. This allows a comparison of solar and ionospheric 27-day signatures without assuming that all wavelengths are impacted by the same 27-day solar rotation periods. The SEA method that was applied to F10.7 and TEC including detection of anomalies, Monte-Carlo significance test and delay estimation is therefore performed with the solar irradiance at each wavelength. This results in different epoch centers and specific signatures for each wavelength. For example, of the specific epoch centers for 60 and 100 nm only 49% overlap in a window of 1 d and only 3.5% are the same. On average, the overlap is 43%. Since these specific epoch centers are also applied to TEC and GTEC, a separate signature is also calculated for each wavelength. The results of this analysis with GTEC are shown in Figure 9. The signatures for the solar irradiance are more symmetric compared to the results in Figure 7 and both minima in the first and second phase of the 27-day period are approximately equal. The deviations at wavelengths of approximately 33 nm and from 90 to 105 nm are also smaller. The adapted approach improves the results and shows the limited applicability of F10.7 to describe the EUV spectrum sufficiently. The corresponding GTEC signatures are well-defined too, but stronger deviations from an ideal sinusoidal fit are observed at different wavelengths.

As signatures in Figure 9 are calculated based on wavelength-dependent epoch centers, the Monte-Carlo method, which was applied to F10.7 and GTEC (see Figure 2), has to be adjusted. For that reason, the amount of random epoch centers is set to the wavelength-dependent values. The fraction of random signatures with greater amplitude than the signatures in Figure 9 is therefore also wavelength-dependent and varies based on the amount of applied epoch centers as well as on the solar irradiance. Figure 10 shows the fraction of the Monte-Carlo significance test and the correlation coefficients of solar irradiance and GTEC at each wavelength. The fractions are generally small (mean of 0.09%) and the calculated signatures are therefore reliable. The correlation of the solar irradiance and GTEC signatures is strong (mean of 0.90), and significant decreases of the correlation are only observed at wavelengths of 33, 70, and 95 nm. But even these results are still moderately correlated. Hence, the full spectrum can be further analyzed.

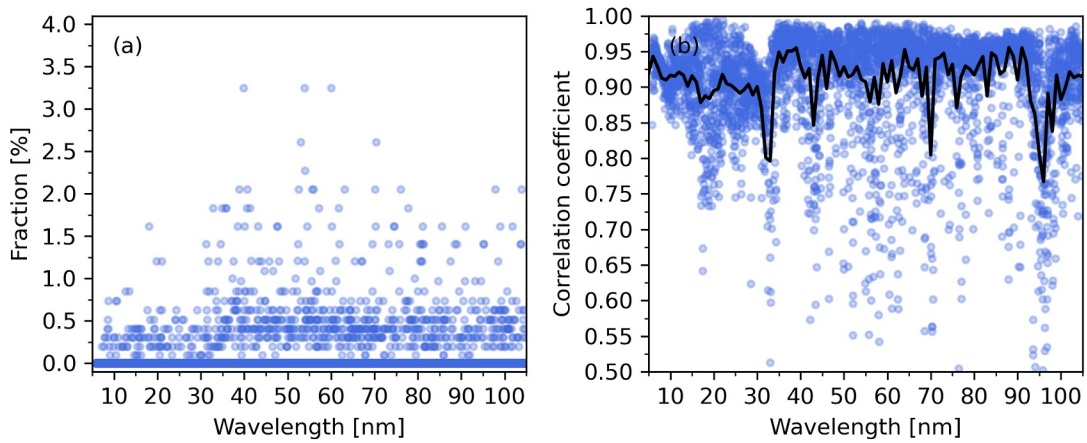

Figure 10. Wavelength-dependent fractions of the Monte-Carlo significance test (a) and correlation coefficients (b) of solar EUV irradiance and GTEC signatures are shown with the blue dots. The black line shows mean correlation coefficients for bins of 1 nm.

The peak time difference and cross-correlation lag of solar EUV irradiance and GTEC signatures in Figure 11 are moderately correlated (correlation coefficient of 0.54), which indicates that a delay similar to the peak time difference occurs at any time of the 27-day period. Both delays are approximately 29 hr at wavelengths from 5 to 30 nm. The delay increases up to 50 and even 75 hr at the wavelength of 33 nm and then decreases to approximately 10–24 hr at wavelengths from 35 to 70 (cross-correlation lag) or 90 nm (peak time difference). An increase of the delay up to 75 and even 100 hr for outliers occurs at wavelengths from 90 to 105 nm. These results are in good agreement with the wavelength-dependent delays reported by Schmölter and von Savigny (2022), but also other studies that used integrated or selected solar EUV irradiance (Ren et al., 2018; Schmölter et al., 2018, 2021). The observed variability is also in good agreement with the understanding of the delayed ionospheric response. Photoionization occurs at wavelengths shorter than 80, 91, 103 nm for N_2, O and O_2, respectively (Fennelly & Torr, 1992). Hence, the smaller delays at wavelengths from 30 to 90 nm are likely related to the immediate production of ions. Schmölter and von Savigny (2022) have also shown a significant increase of the delay at even longer wavelengths, which is due photodissociation occurring at wavelengths shorter than 242 nm. These varying response times of the ionospheric plasma are further reflected with height-dependent electron density changes (Schmölter & von Savigny, 2022) and the integrated response via TEC (see Figure 2). The results in Figures 9 and 11 are in good agreement with the established understanding of the delayed ionospheric response and, based on this, the temporal and spatial variations during low and high solar activity are investigated in more detail below.

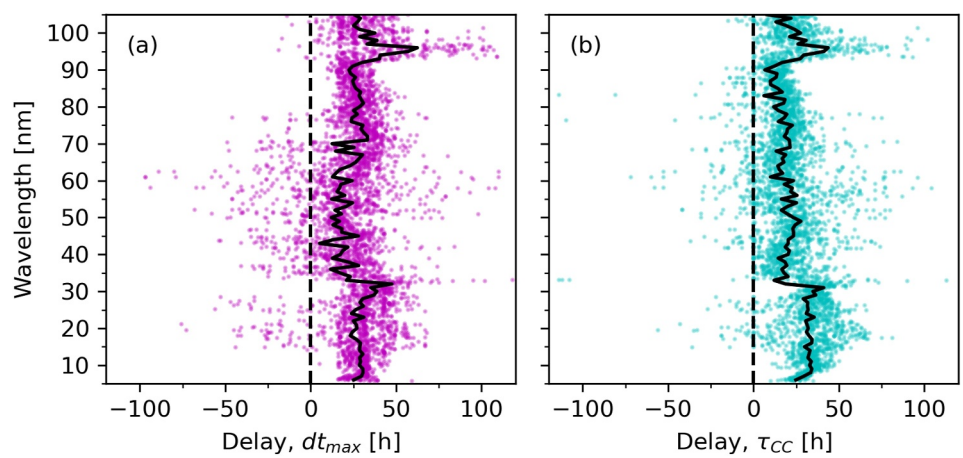

Figure 11. Wavelength-dependent peak time difference (a) and cross-correlation lag (b) of solar EUV irradiance and GTEC signatures are shown with the colored dots. The black lines show mean values for bins of 1 nm.

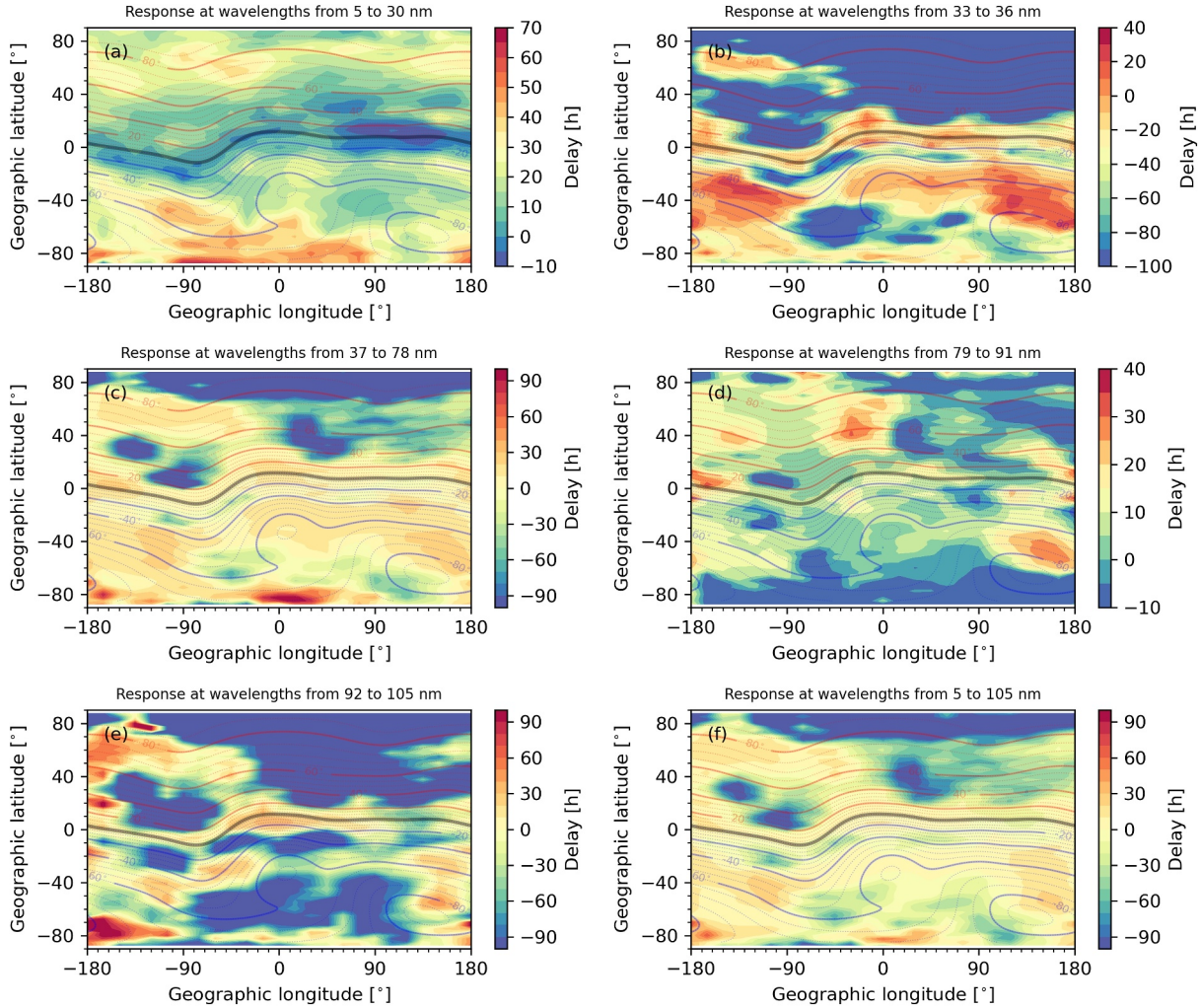

Figure 12. Cross-correlation lags (delay) via the SEA method at different wavelength ranges and World Magnetic Model (WMM) inclination (red and blue lines) are shown.

Discussing the spatial changes at each wavelength (even for bins of 1 nm) is not necessary, as manual inspections shows that the identified wavelength ranges with similar variability in Figures 10 and 11 also have common spatial structures. For that reason, Figure 12 shows the latitude- and longitude-dependent mean cross-correlation lags at wavelengths from 5 to 30 nm (increase at short wavelengths), from 33 to 36 nm (strong deviations), from 37 to 78 nm, from 79 to 91 nm (increase at longer wavelengths), from 92 to 105 nm (strong deviations) and from 5 to 105 nm (full spectrum). In three of the wavelength ranges (see Figures 12b, 12c, and 12e) as well as the full spectrum (Figure 12f), the minimum at the magnetic equator appears to be shifted southwards, which is particularly noticeable for the equatorial crest. This deviation is caused by a bias of the wavelength-dependent epoch centers toward the Southern hemisphere summer (14%, 23%, and 20%). In addition to the shift, this is likely also causing the partly negative delays in Figures 12b and 12e in the Northern hemisphere. A smaller impact of the solar activity is expected for these regions during winter. Nevertheless, the spatial structures of delays at wavelengths from 33 to 36 nm, from 37 to 78 nm and from 92 to 105 nm are similar compared to the results based on F10.7 (see Figure 3).

Different delay variability is observed at wavelengths from 79 to 91 nm. These delays are longer than average at mid-latitudes and the equator. Decreased delays are observed at the equatorial crest opposed to the other results. This different variability occurs due to absorption processes changing in favor of O_2 at this wavelength range and a correlation with the lower ionosphere rather than the peak is expected (Schmölter et al., 2022). The absorption

processes may be further affected by the fountain effect (Lin et al., 2007; Maruyama, 1996) that has varying impacts on the delayed ionospheric response (Vaishnav, Schmölter, et al., 2021).

The delay at wavelengths from 5 to 30 nm in Figure 12 has its minimum along the geomagnetic equator and increases with latitude. Increases at the equatorial crest are much less pronounced. Thus, a stronger correlation with solar activity (via solar zenith angle) is implied, but different short- and long-term changes may also be important (Chen et al., 2012).

Figures 3 and 12 show that spatial features discussed in preceding studies must be carefully compared as the applied solar proxy or solar EUV measurements can significantly change the results. Modeling studies using the solar proxy F10.7 (Schmölter et al., 2022; Vaishnav et al., 2018, 2019; Vaishnav, Jacobi, et al., 2021; Vaishnav, Schmölter, et al., 2021) via solar flux models (e.g., EUVAC) describe spatial variations like the results based on the full spectrum (see Figure 12f) or response at wavelengths from 37 to 78 nm (see Figure 12b). Studies using the solar proxy Q_{EUV} (Schmölter et al., 2021; Vaishnav et al., 2023), which describes the integrated solar EUV irradiance at wavelengths shorter than 45 nm (Eastes et al., 2017), or Solar and Heliospheric Observatory (SOHO) Solar EUV Monitor (SEM) measurements with two bands from 26 to 34 nm and from 0.1 to 50 nm (Judge et al., 1998) are more difficult to interpret, since these wavelength ranges integrate different features. Wavelength-dependent analyses (Schmölter & von Savigny, 2022) are complex, but offer a reference to studies using solar EUV at specific wavelength ranges.

6. Solar Activity Driven Delay Variability Analyzed via Wavelength-Dependent EUV Irradiance

The impact of solar activity is estimated by categorizing the wavelength-dependent epoch centers according to the general solar activity level. For that purpose, the mean spectral solar irradiance for wavelengths longer than 33 nm is calculated. The shorter wavelengths are excluded to avoid differences before and after 26 May 2014. The resulting mean irradiance is well correlated with F10.7 (correlation coefficient of 0.94) and therefore a corresponding estimate for the solar proxy can be provided as well. This in turn allows a comparison to the result in Figure 4. The mean irradiance from $1.75 \cdot 10^{-5}$ to $2.75 \cdot 10^{-5}$ $W{\cdot}m^{-2}{\cdot}nm^{-1}$ is analyzed (approximately 70–180 sfu) and the SEA method is applied, if atleast 10 epoch centers are available. The resulting wavelength- and mean irradiance-dependent signatures are used to calculate the peak time difference and the cross-correlation lag.

Figure 13 shows the calculated peak time differences and cross-correlation lags. Most noticeable for the peak time difference (Figure 13a) are the approximately constant delays at mean irradiance from $2.1 \cdot 10^{-5}$ to $2.6 \cdot 10^{-5}$ $W{\cdot}m^{-2}{\cdot}nm^{-1}$ (120–160 sfu) and wavelength ranges shorter than 90 nm. From 10 to 30 nm, from 40 to 60 nm and from 65 to 85 nm, mean delays of 28, 20, and 26 hr are observed, respectively (see e.g. Figure 13c). The corresponding correlations for these delays are strong (correlation coefficient of 0.96). At longer wavelengths (90–100 nm), the peak time difference decreases from approximately 55 to 23 hr at mean irradiance from $2.1 \cdot 10^{-5}$ to $2.6 \cdot 10^{-5}$ $W{\cdot}m^{-2}{\cdot}nm^{-1}$ (120–160 sfu) and therefore the delay approaches the observed delay at shorter wavelengths. At higher mean irradiance, the correlation decreases (correlation coefficient of 0.90) and the peak time differences increase (especially at wavelengths longer than 60 nm). At lower mean irradiance (below $2.1 \cdot 10^{-5}$ $W{\cdot}m^{-2}{\cdot}nm^{-1}$), the peak time differences vary strongly and especially at wavelengths from 65 to 85 nm and from 90 to 100 nm the correlation decreases strongly (correlation coefficient 0.56), while the delay increases up to 69 hr. At wavelengths from 40 to 60 nm, the correlation decreases less strong (correlation coefficient of 0.85) and a decrease of the delays is observed.

The cross-correlation lag (Figure 13b) is less susceptible to the decreases of the correlation and therefore smaller deviations occurs at low and high mean irradiance. At wavelengths from 65 to 85 nm and from 90 to 100 nm, the cross-correlations lags are approximately constant at 15 and 27 hr, but at wavelengths from 10 to 30 nm and from 40 to 60 nm, a continuous increase of the delay from 17 to 29 hr and from −34 to 29 hr is observed, respectively. These increases are slower (0.15 and 0.63 hr/sfu) compared to the increase in Figure 4, which indicates that the different absorption processes (dependent on wavelength) cause changes in the ionospheric plasma which combined favor stronger accumulation.

Generally, increasing photoionization rates of all major species are expected with increasing mean solar irradiance as more energy is deposited in the upper atmosphere. This in turn would increase the accumulation of ionospheric plasma and if no further processes are considered, then an increasing delay should be observed at all

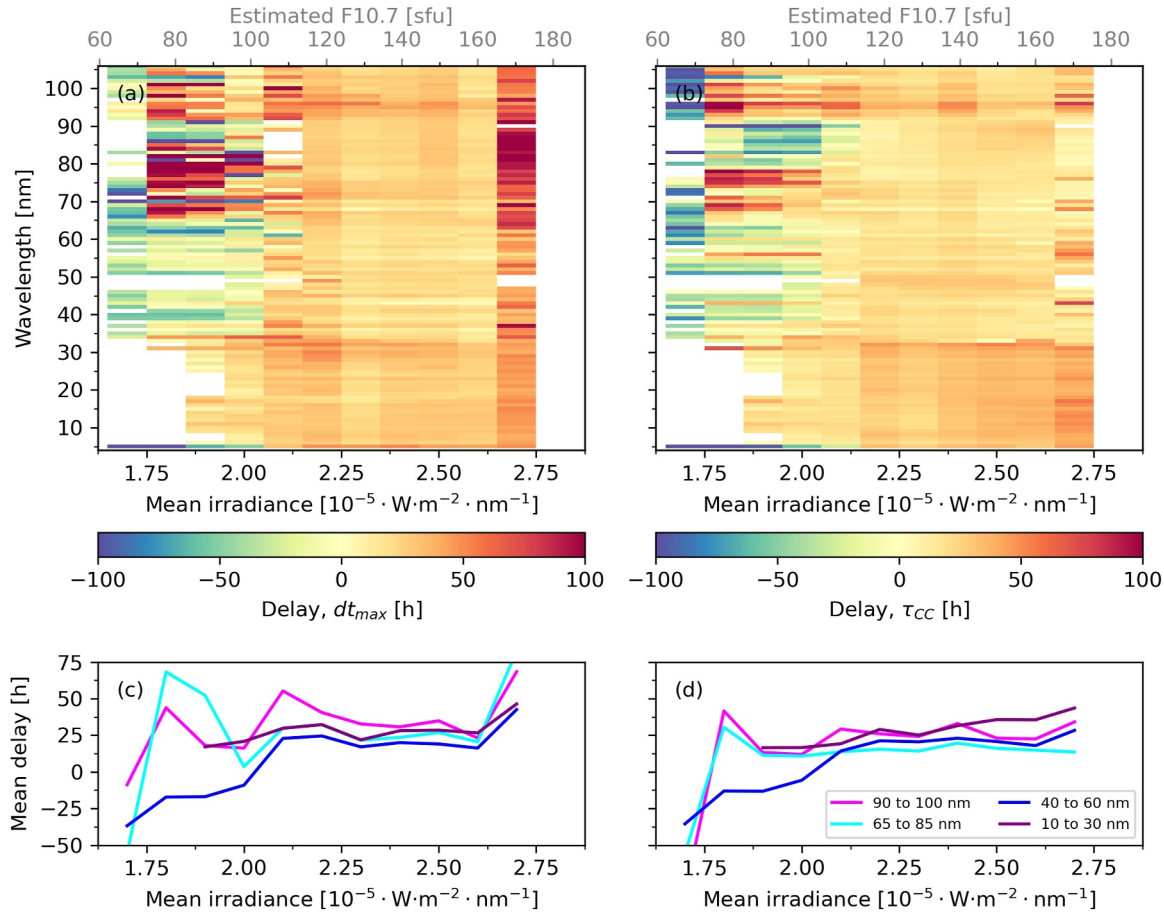

Figure 13. Irradiance- and wavelength-dependent peak time difference (a) and cross-correlation lag (b) of solar EUV irradiance and GTEC signatures are shown. The colored lines (c, d) show mean values for selected wavelength ranges.

wavelengths. But, composition changes (e.g. photodissociation of O_2 to O) also increase with increasing mean solar irradiance and therefore the photoionization rates are further affected (e.g., increased photoionization of O, but decreased photoionization of O_2). Additionally, the height of the ionospheric plasma increases with increasing mean solar irradiance, which changes the recombination rates as well (Ashworth et al., 1956). These changes generally favor the production of O^+, as the composition changes in favor of O, the ionization rate is increased and the plasma peak is higher. Figure 13b reflects this with the increasing delays at wavelengths shorter than 80 nm (absorption via photoionization of O). The changes of the production of O_2^+ are more complex, as the amount of O_2 is decreased, and the ionization rate could be differently affected. Figure 13b indicates that there are no significant changes with the constant delays at wavelengths shorter than 103 nm (absorption via photoionization of O_2) and Figure 13a indicates even a decreased production of O_2^+ (less accumulation) with decreasing delays. Furthermore, the density of O_2 and N_2 increases due to heating when the solar EUV radiation is absorbed, which in turn increases recombination rates. This response is slower than the increase of the ionization rate (Ren et al., 2018) and contributes to the delayed ionospheric response as well. For these reasons, the results are in good agreement with the understanding of major processes driving the delayed ionospheric response (Ren et al., 2018; Schmölter & von Savigny, 2022) and further highlight the importance of the ionospheric composition for the delay.

An example for the latitude- and longitude-dependent delayed ionospheric response is calculated at wavelengths from 5 to 30 nm to investigate spatial features of the observed increase according to GTEC in Figure 13b. At the selected wavelength range solar irradiance is observed from approximately 10^{-6} to 10^{-3} $W \cdot m^{-2} \cdot nm^{-1}$ and the epoch centers are categorized in six groups (logarithmic scale) to present the changes according to increasing solar activity. Figure 14 shows the SEA results for the six solar irradiance levels. The mean of the delay maps

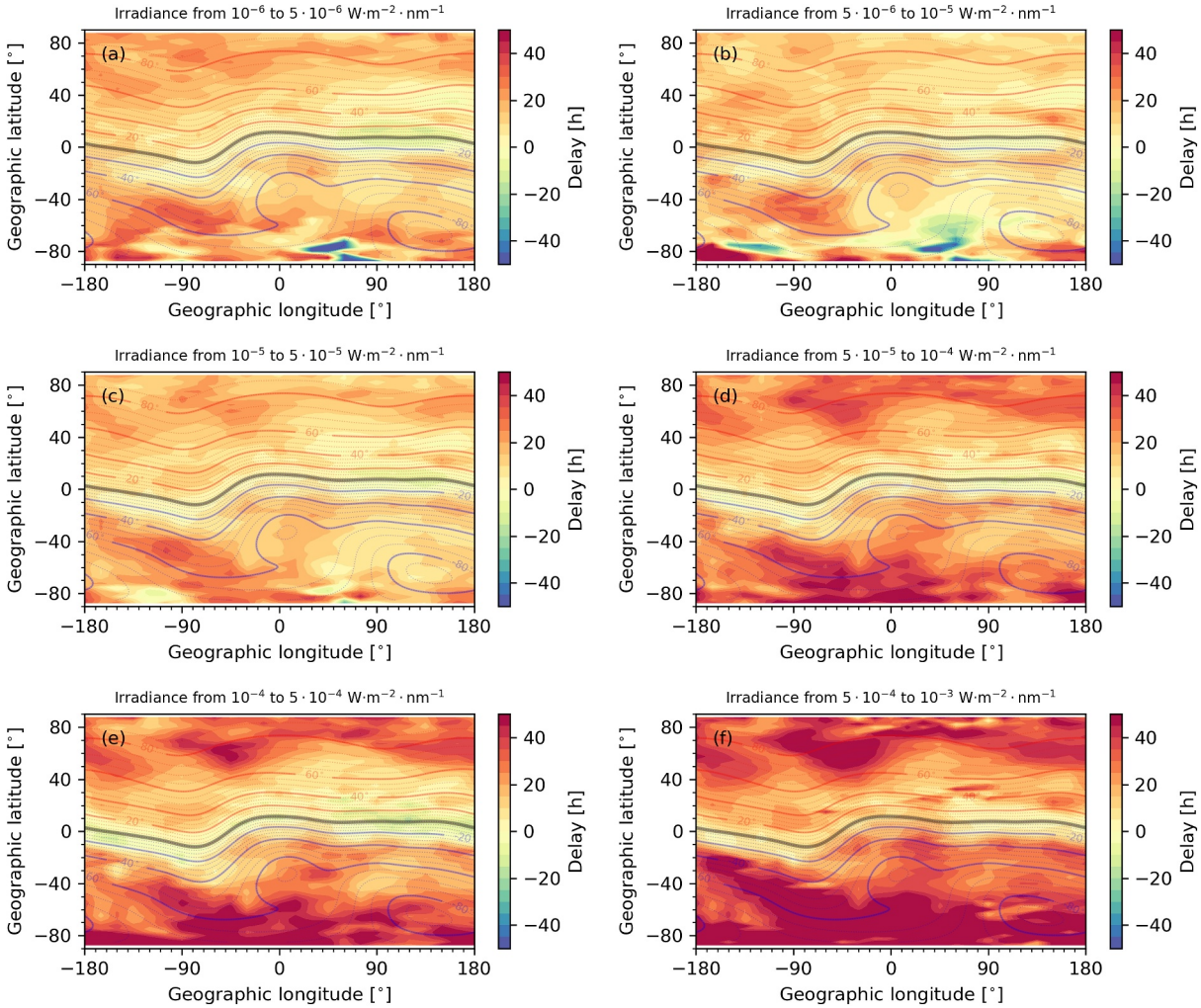

Figure 14. Cross-correlation lags (delay) via the SEA method at different solar irradiance levels (wavelength range from 5 to 30 nm) and World Magnetic Model (WMM) inclination (red and blue lines) are shown.

increases noticeable from 12 to 33 hr with increasing solar irradiance level, but the increase is not evenly distributed and spatial features occur. At the geomagnetic equator, the delay increases from approximately 0 to 10 hr from the lowest to the highest solar irradiance level and a strong difference is observed for the two highest levels (5 hr). At the equatorial crest, a similar increase from 8 to 18 hr is observed. These small increases of the delay with increasing solar irradiance occur, as recombination is likely increased in these regions by the transport of plasma to lower heights (Ashworth et al., 1956) due to the fountain effect (Lin et al., 2007; Maruyama, 1996). At low- and mid-latitudes the delay is not affected by these processes and increases with increasing latitude. This increase is enhanced for higher solar irradiance levels and delays increase approximately from 10 to 40 hr. The longest delays and strongest increase of the delay with increasing solar irradiance occurs at high-latitudes with delays up to 50 hr in the Southern hemisphere.

The increase of the delayed ionospheric response with solar activity level reported by preceding studies (Schmölter et al., 2018; Vaishnav, Schmölter, et al., 2021) is confirmed with the SEA method (see e.g. Figures 5 and 14). Composition changes via photodissociation of O_2 (Schmölter & von Savigny, 2022) and changes of the solar zenith angle (Schmölter et al., 2018) are indicated as major impacts on the delay due to the strong dependence on latitude. An increase of the deposited energy q_E occurs in the upper atmosphere as the solar EUV irradiance I increases according to

$$q_E = I \cdot e^{-ch(\chi,h)} \sim I \cdot e^{-\sec(\chi)}. \quad (1)$$

The Chapman function $ch(\chi, h)$ reflects the shape of the atmosphere and is most importantly dependent on height h and solar zenith angle χ, which in turn depends on geographic latitude and local time. Increases of the photoionization and photodissociation rates are therefore latitude-dependent too and as more ionospheric plasma is created, the recombination rates increase as well. An imbalance of plasma production and loss (resulting in the delayed ionospheric response) is introduced via the photodissociation of O_2, which increases the production of plasma at the ionosphere peak via O and decreases the loss in the lower ionosphere via O_2 but also N_2 (Schmölter & von Savigny, 2022). The height of ionospheric plasma profile also increases with solar activity level (Rao et al., 2014), which further decreases the recombination rates (Ashworth et al., 1956).

At the equator, the ionospheric plasma is impacted by the fountain effect, which causes the equatorial ionization anomaly. The amount of plasma of the anomaly and its height increases during high solar activity and the local response to the 27-day solar rotation period follows this trend (Li et al., 2018). The delayed ionospheric response along the equator in Figures 5 and 12c reflects these changes well, but the results at wavelengths from 5 to 30 nm in Figure 12a require further analysis in the future. Of particular interest would be the investigation of height-dependent composition changes in the anomaly (Balan, Liu, & Le, 2018; Balan, Souza, & Bailey, 2018), which in turn would impact the interaction with solar EUV.

7. Local Time-Dependent Changes of the Delay

For the analysis with F10.7 and GTEC, no influence of local time is expected, as the data are independent of diurnal variations and the SEA method would remove any small effect. Similarly, the effect is also removed for latitude- and longitude-dependent results, and the good correlations confirm that the SEA method is appropriate. However, a local time-dependent analysis can be performed by selecting the corresponding LT hours. This initially results in time series with a resolution of 1 d, but by using the SEA method, averaged delays with a resolution better than 1 d are estimated.

Local time- and wavelength-dependent delays are shown in Figure 15. Increased delays are approximately observed from 15:00 to 21:00 LT and from 0:00 to 7:00 LT (semi-diurnal variation) and generally the delay is 3 hr longer at night from 18:00 to 6:00 LT (diurnal variation). These periods vary at different wavelengths and particular at wavelengths longer than 75 nm different variability is observed. At wavelengths from 79 to 90 nm, the delay is increased from 16:00 to 7:00 LT without a decrease during local midnight. At even longer wavelengths, strong deviations occur and the diurnal and semi-diurnal variation are less pronounced. Additionally, a significant increase of the cross-correlation lag is observed at wavelengths from 50 to 80 nm after local midnight from 0:00 to 6:00 LT.

The increased delayed ionospheric response during local noon is related to the TEC maximum that occurs in this period (Liu & Chen, 2009), as stronger ionization than recombination rates are expected. During nighttime, the recombination dominates and the plasma in the lower ionosphere decreases fast, which in turn increases the height of the ionosphere peak (Kalita et al., 2015; Sethi et al., 2004). The maximum height is expected during midnight. The remaining plasma recombines at a slower rate (Ashworth et al., 1956) and the increased delay until morning occurs. Thus, the local time-dependent changes are in good agreement with the major processes driving the delayed ionospheric response and the 27-day signature is superimposed with a diurnal cycle.

Figure 16 shows the latitude- and longitude-dependent cross-correlation lags at 6:00, 12:00, 18:00 and 0:00 LT (wavelength range from 37 to 78 nm). There are no significant differences at 6:00 and 12:00 LT, but increasing delays are observed at 18:00 and 0:00 LT. The spatial variations show again a strong dependence on latitude, but the delay range is much smaller than for solar activity changes (see Figure 14).

8. Impact of Geomagnetic Activity on the SEA Results

Geomagnetic activity is a strong driver of ionospheric disturbances and long-term changes (Field & Rishbeth, 1997; Fuller-Rowell et al., 1994, 2000; Laštovička, 2005), and correlates with solar activity cycles (Du, 2011; Legrand & Simon, 1981). For that reason, the geomagnetic activity has to be considered as a possible impact on the results via the SEA method, as a geomagnetic activity signature could be superimposed with the solar activity changes. For that reason, the SEA signature of Kp is calculated based on the applied epoch centers. Figure 17 shows the Kp signatures and the mean signature. While some Kp signatures include moderate and strong geomagnetic activity, the mean signature is constant at approximately 1.52. Thus, there is no superimposed

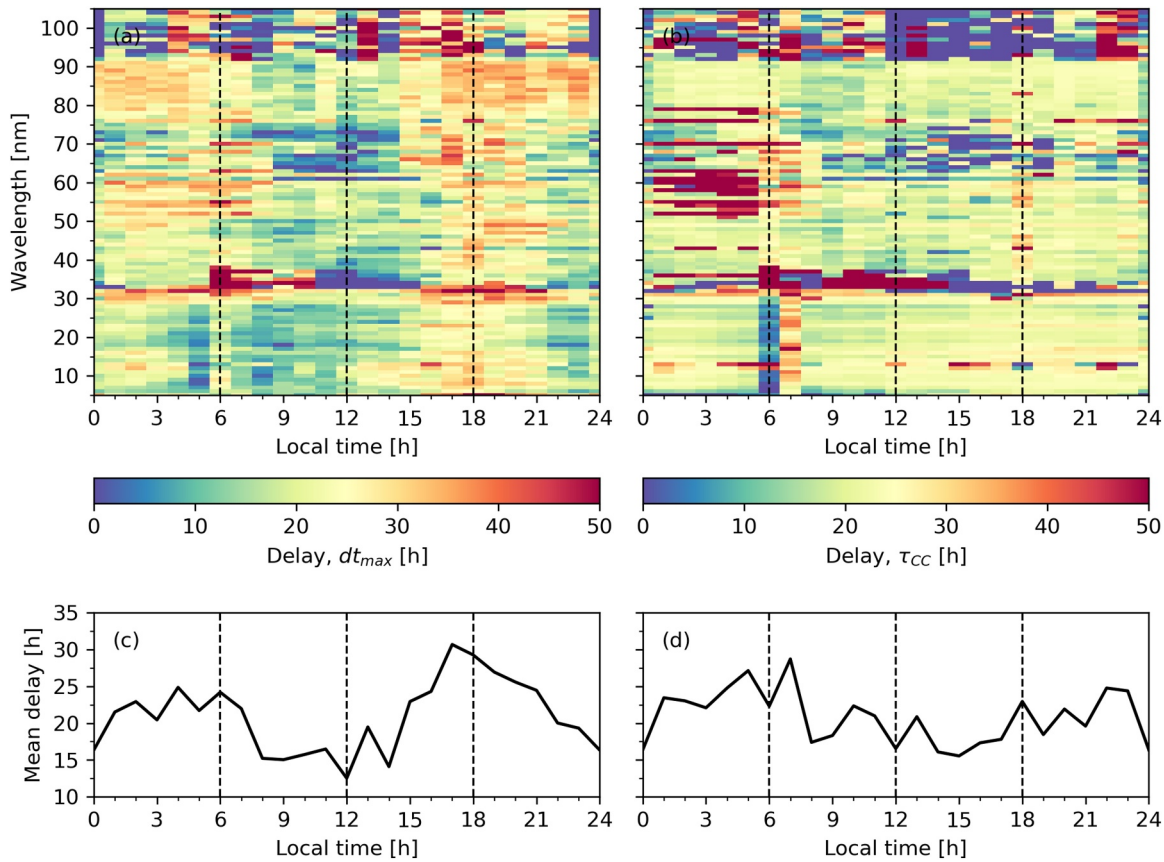

Figure 15. Local time- and wavelength-dependent peak time difference (a) and cross-correlation lag (b) of solar EUV irradiance and local time-dependent TEC signatures are shown. The black lines (c, d) show mean values according to local time.

trend due to geomagnetic activity and the estimated SEA signatures based on F10.7 and solar EUV measurements reflect results during low geomagnetic activity. This confirms that the presented results show only the response to solar EUV changes.

9. Discussion

The present study investigated the spatial and temporal variations of the delayed ionospheric response at different solar activity levels. The results based on F10.7 are in good agreement with preceding studies using the solar proxy for ionospheric modeling (Ren et al., 2018; Schmölter et al., 2022; Vaishnav et al., 2018, 2019, 2023; Vaishnav, Jacobi, et al., 2021; Vaishnav, Schmölter, et al., 2021) and are of interest, since modeling via solar flux models based on F10.7 is commonly applied. The wavelength-dependent results provide a more comprehensive insight to the various processes impacting the delayed ionospheric response. The local analysis is also important, as global indices have strong deviations (see Figure 13) due to the averaging of various latitude-, longitude- and local time- dependent processes.

The results of the present study are limited to a narrow band of solar activity oscillations (27-day solar rotation period), but the overall ionospheric response is impacted by shorter and longer oscillations as well. The wavelength-dependent fast Fourier transform of the solar irradiance in Figure 18 shows that the 27-day signatures are a clear contribution at all wavelengths. Nevertheless, the variability is complex and an analysis considering the various signatures would be of interest.

The amplitudes of 27-day signatures vary from 7.5 to 123.8 sfu for F10.7 and correlate strongly with the mean solar activity level (correlation coefficient of 0.86). The solar EUV amplitude variations are dependent on wavelength, vary up to $2 \cdot 10^{-3}$ W·m^{-2}·nm^{-1} and are only weakly correlated with the solar activity level (mean correlation coefficient of 0.21). Hence, a separate analysis based on amplitude could be of interest as weaker or

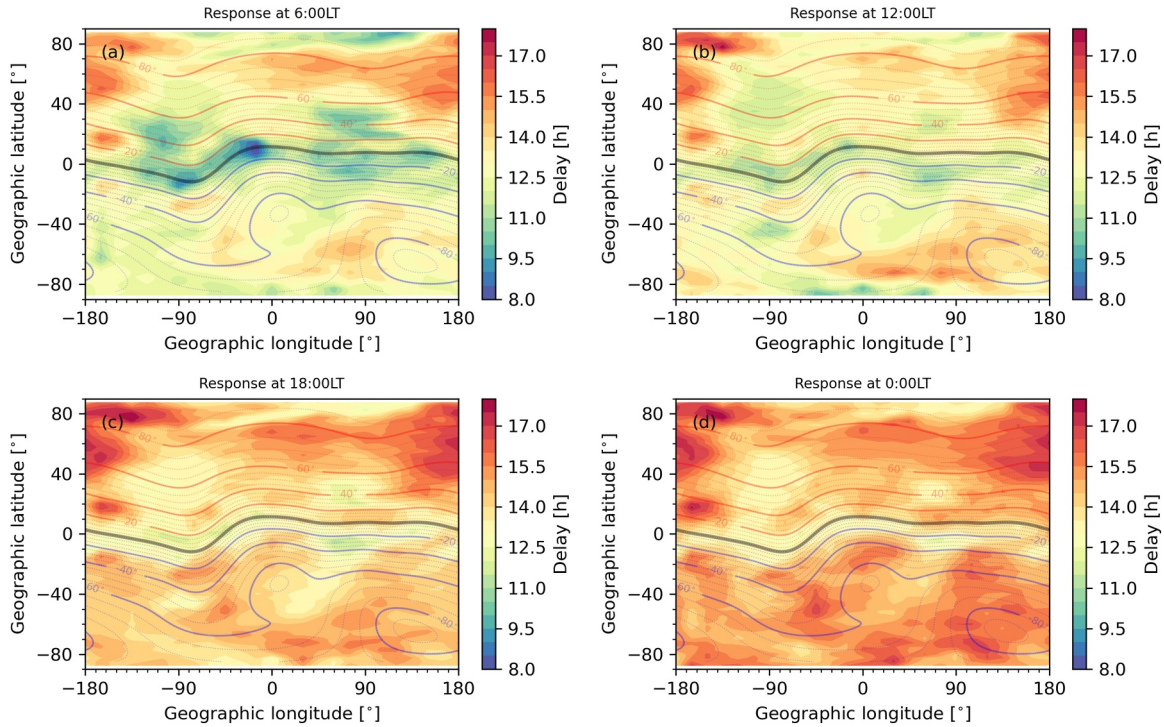

Figure 16. Cross-correlation lags (delay) via the SEA method at different local hours (wavelength range from 37 to 78 nm) and World Magnetic Model (WMM) inclination (red and blue lines) are shown.

stronger variations of the ionization and recombination rates have a different impact on the delayed ionospheric response. Schmölter et al. (2021) presented these processes with two example 27-day solar rotation periods, but a statistical analysis including a greater variety may be of interest for future studies.

Schmölter and von Savigny (2022) investigated the wavelength- and height-dependent delayed ionospheric response, while the present studied analyzed wavelength-, latitude-, longitude- and local time-dependent changes in more detail. Both analysis based on observations provide insight to the processes driving the response, but a combined analysis of height-dependent spatial changes would allow to identify processes in specific regions of the ionosphere. Such an analysis requires global 3-dimensional electron density data though, which can only be provided by including appropriate modeling and assimilation of observations.

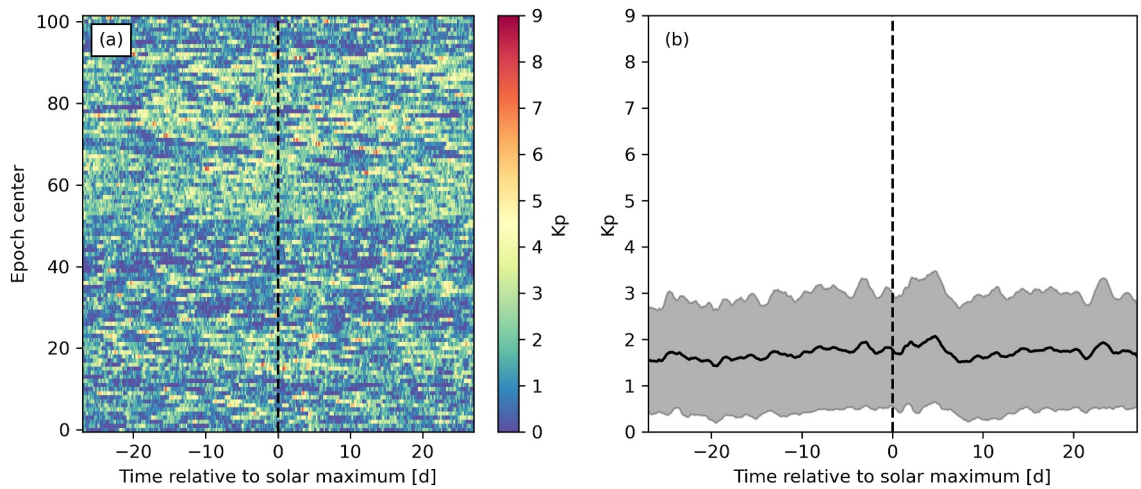

Figure 17. Kp signatures (a) for each epoch and the mean Kp signature (b) are shown. The corresponding standard deviation is shown with the gray shading.

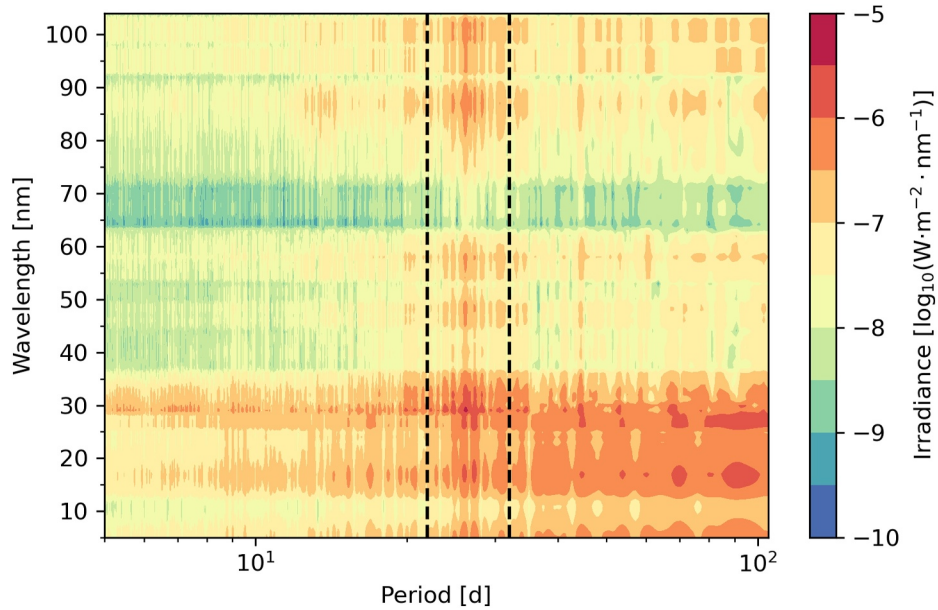

Figure 18. Wavelength-dependent fast Fourier transform of the solar EUV irradiance is shown. The dashed lines mark periods from 22 to 32 d.

10. Conclusion

The present study investigated the delayed ionospheric response (peak time difference and cross-correlation lag of 27-day signatures) via the SEA method with the solar proxy F10.7 and SDO/EVE solar EUV irradiance as well as local and global TEC. The results extend preceding studies (Schmölter & von Savigny, 2022) and quantify the solar activity-dependent changes of the delay.

Latitude- and longitude-dependent SEA results for F10.7 and TEC show a strong increase of the delayed ionospheric toward mid-latitudes with especially strong enchantments at the equatorial ionization anomaly during high solar activity (see Figure 5). Globally, an increase of the delay from 15 to 55 hr is observed for increasing F10.7 from 100 to 160 sfu (mean of 27-day solar rotation period). The increase strongly correlates with geographic latitude (see Figure 6) due to the solar zenith angle dependent absorption (see Equation 1), which causes an increase of ionization rates toward the equator (Schmölter et al., 2018). Heating due to this absorption causes an increase of the density of O_2 and N_2, which in turn increases the recombination rates toward the equator as well. This increase is slower though (Ren et al., 2018) causing the delayed ionospheric response as reported in preceding studies.

Wavelength-dependent SEA results for F10.7 and solar EUV show varying delays throughout the EUV spectrum (see Figure 8). Schmölter and von Savigny (2022) reported these differences with TIMED/SEE measurements and the present study confirms the results with SDO/EVE measurements. While an investigation with F10.7 is of interest due to the extensive use of the solar proxy for studies with ionosphere models (Ren et al., 2018; Schmölter et al., 2022; Vaishnav et al., 2018, 2019, 2023; Vaishnav, Jacobi, et al., 2021; Vaishnav, Schmölter, et al., 2021), the complex variability of solar EUV can only be partially reflected.

Wavelength-, latitude- and longitude-dependent SEA results for solar EUV and TEC show the temporal and spatial variations of the delayed ionospheric response in more detail (see Figures 11, 12, and 14). Different variations are observed at wavelengths from 5 to 30 nm (increase at short wavelengths), from 33 to 36 nm (strong deviations), from 37 to 78 nm (agreement with mean), from 79 to 91 nm (increase at longer wavelengths) and from 92 to 105 nm (strong deviations). These variations reflect the different absorption processes of the three major species (N_2, O and O_2) and their respective impact on the delay (Schmölter & von Savigny, 2022). The spatial variations are also different for these EUV bands, but the response for the integrated spectrum is similar to the response via F10.7 (see Figures 3 and 12f). The change according to mean solar irradiance is described with the GTEC response (see Figure 13) and the cross-correlation lags show an increase of the delay with increasing

solar irradiance level at wavelengths shorter than 80 nm and complex variations at longer wavelengths. These changes also have spatial features (see Figure 14) with enhancements of the delay toward high latitudes. Local-time dependent analyses show variability of the delayed ionospheric response with increases from 15:00 to 21:00 LT and from 0:00 to 7:00 LT, but the delay range is smaller compared to solar activity driven variations. The results confirm that the delayed ionospheric response is dominated by the rates of ionization and recombination during day time (Ren et al., 2018; Schmölter & von Savigny, 2022), and by recombination and dynamic processes during nighttime.

Future studies could extend the SEA method to cover all dimensions of interest, since time-, wavelength-, latitude-, longitude- and height-dependent results would allow to identify the extent of specific processes (e.g., photoionization of O and O_2 via wavelength and height or plasma transport in equatorial ionization anomaly via latitude and height). All of these are covered separately with observational results in the present study and results by Schmölter and von Savigny (2022), but a combined analysis could provide an comprehensive reference for modeling efforts on the delayed ionospheric response.

Data Availability Statement

OMNI data were obtained from the GSFC/SPDF OMNIWeb interface at https://omniweb.gsfc.nasa.gov/. SDO/EVE data were obtained from the LASP web interface at https://lasp.colorado.edu/eve/data/. IGS TEC maps were obtained from the IGS web interface at https://igs.org/products/. WMM data were obtained from the WMM web calculator at https://www.ncei.noaa.gov/products/world-magnetic-model.

Acknowledgments
This study was supported by Deutsche Forschungsgemeinschaft (DFG) through Grants JA 836/48-1 and SCHM 3761/1-1. Open Access funding enabled and organized by Projekt DEAL.

References

Ashworth, R. J., Schmerling, E. R., & Setty, C. S. G. K. (1956). The rates of production and loss of electrons in the F region of the ionosphere. *Philosophical Transactions of the Royal Society of London - Series A: Mathematical and Physical Sciences*, *248*(956), 621–642. https://doi.org/10.1098/rsta.1956.0012

Balan, N., Liu, L., & Le, H. (2018). A brief review of equatorial ionization anomaly and ionospheric irregularities. *Earth and Planetary Physics*, *2*(4), 1–19. https://doi.org/10.26464/epp2018025

Balan, N., Souza, J., & Bailey, G. J. (2018). Recent developments in the understanding of equatorial ionization anomaly: A review. *Journal of Atmospheric and Solar-Terrestrial Physics*, *171*, 3–11. https://doi.org/10.1016/j.jastp.2017.06.020

Chen, Y., Liu, L., & Wan, W. (2012). The discrepancy in solar EUV-proxy correlations on solar cycle and solar rotation timescales and its manifestation in the ionosphere. *Journal of Geophysical Research*, *117*(A3). https://doi.org/10.1029/2011ja017224

Didkovsky, L., Judge, D., Wieman, S., Woods, T., & Jones, A. (2009). EUV SpectroPhotometer (ESP) in extreme ultraviolet variability experiment (EVE): Algorithms and calibrations. *Solar Physics*, *275*(1–2), 179–205. https://doi.org/10.1007/s11207-009-9485-8

Du, Z. L. (2011). The correlation between solar and geomagnetic activity—Part 2: Long-term trends. *Annales Geophysicae*, *29*(8), 1341–1348. https://doi.org/10.5194/angeo-29-1341-2011

Eastes, R. W., McClintock, W. E., Burns, A. G., Anderson, D. N., Andersson, L., Codrescu, M., et al. (2017). The global-scale observations of the limb and disk (GOLD) mission. *Space Science Reviews*, *212*(1–2), 383–408. https://doi.org/10.1007/s11214-017-0392-2

Fennelly, J. A., & Torr, D. G. (1992). Photoionization and photoabsorption cross sections of O, N_2, O_2, and N for aeronomic calculations. *Atomic Data and Nuclear Data Tables*, *51*(2), 321–363. https://doi.org/10.1016/0092-640x(92)90004-2

Field, P. R., & Rishbeth, H. (1997). The response of the ionospheric F2-layer to geomagnetic activity: An analysis of worldwide data. *Journal of Atmospheric and Solar-Terrestrial Physics*, *59*(2), 163–180. https://doi.org/10.1016/S1364-6826(96)00085-5

Fuller-Rowell, T. J., Codrescu, M. C., & Wilkinson, P. (2000). Quantitative modeling of the ionospheric response to geomagnetic activity. *Annales Geophysicae*, *18*(7), 766–781. https://doi.org/10.1007/s00585-000-0766-7

Fuller-Rowell, T. J., Codrescu, M. V., Moffett, R. J., & Quegan, S. (1994). Response of the thermosphere and ionosphere to geomagnetic storms. *Journal of Geophysical Research*, *99*(A3), 3893–3914. https://doi.org/10.1029/93ja02015

GFZ. (2023). German Research Centre for Geosciences—geomagnetic Kp index [Dataset]. Retrieved from https://kp.gfz-potsdam.de/

Hernández-Pajares, M., Juan, J. M., Sanz, J., Orus, R., Garcia-Rigo, A., Feltens, J., et al. (2009). The IGS VTEC maps: A reliable source of ionospheric information since 1998. *Journal of Geodesy*, *83*(3–4), 263–275. https://doi.org/10.1007/s00190-008-0266-1

Hock, R. A., Chamberlin, P. C., Woods, T. N., Crotser, D., Eparvier, F. G., Woodraska, D. L., & Woods, E. C. (2010). Extreme ultraviolet variability experiment (EVE) multiple EUV grating spectrographs (MEGS): Radiometric calibrations and results. *Solar Physics*, *275*(1–2), 145–178. https://doi.org/10.1007/s11207-010-9520-9

Hunsucker, R. D., & Hargreaves, J. K. (2007). *The high-latitude ionosphere and its effects on radio propagation*. Cambridge University Press.

IGS. (2023). International global navigation satellite system service—Data [Dataset]. Retrieved from https://cddis.nasa.gov/archive/gnss/data/highrate/

Jakowski, N., Fichtelmann, B., & Jungstand, A. (1991). Solar activity control of ionospheric and thermospheric processes. *Journal of Atmospheric and Terrestrial Physics*, *53*(11–12), 1125–1130. https://doi.org/10.1016/0021-9169(91)90061-b

Judge, D. L., McMullin, D. R., Ogawa, H. S., Hovestadt, D., Klecker, B., Hilchenbach, M., et al. (1998). First solar EUV irradiances obtained from SOHO by the CELIAS/SEM. In *Solar electromagnetic radiation study for solar cycle 22* (pp. 161–173). Springer Netherlands. https://doi.org/10.1007/978-94-011-5000-2_12

Kalita, B. R., Bhuyan, P. K., & Yoshikawa, A. (2015). NmF2 and hmF2 measurements at 95°E and 127°E around the EIA northern crest during 2010–2014. *Earth Planets and Space*, *67*(1), 186. https://doi.org/10.1186/s40623-015-0355-3

LASP. (2023). Laboratory for atmospheric and space physics—Home page of the extreme ultraviolet variability experiment (EVE) [Dataset]. Retrieved from https://lasp.colorado.edu/eve/data/

Laštovička, J. (2005). On the role of solar and geomagnetic activity in long-term trends in the atmosphere–ionosphere system. *Journal of Atmospheric and Solar-Terrestrial Physics*, *67*(1–2), 83–92. https://doi.org/10.1016/j.jastp.2004.07.019

Legrand, J. P., & Simon, P. A. (1981). Ten cycles of solar and geomagnetic activity. *Solar Physics*, *70*(1), 173–195. https://doi.org/10.1007/bf00154399

Lei, J., Forbes, J. M., Liu, H.-L., Dou, X., Xue, X., Li, T., & Luan, X. (2011). Latitudinal variations of middle thermosphere: Observations and modeling. *Journal of Geophysical Research*, *116*(A12). https://doi.org/10.1029/2011ja017067

Li, K., Lin, L., Bui, X., & Liang, M. (2018). The 11 Year solar cycle response of the equatorial ionization anomaly observed by GPS radio occultation. *Journal of Geophysical Research: Space Physics*, *123*(1), 848–861. https://doi.org/10.1002/2017ja024634

Lin, C. H., Hsiao, C. C., Liu, J. Y., & Liu, C. H. (2007). Longitudinal structure of the equatorial ionosphere: Time evolution of the four-peaked EIA structure. *Journal of Geophysical Research*, *112*(A12). https://doi.org/10.1029/2007ja012455

Liu, L., & Chen, Y. (2009). Statistical analysis of solar activity variations of total electron content derived at Jet Propulsion Laboratory from GPS observations. *Journal of Geophysical Research*, *114*(A10). https://doi.org/10.1029/2009ja014533

Maruyama, T. (1996). Modeling study of equatorial ionospheric height and spread F occurrence. *Journal of Geophysical Research*, *101*(A3), 5157–5163. https://doi.org/10.1029/95ja03469

Matzka, J., Bronkalla, O., Tornow, K., Elger, K., & Stolle, C. (2021). Geomagnetic Kp index. *GFZ Data Services*. https://doi.org/10.5880/KP.0001

Matzka, J., Stolle, C., Yamazaki, Y., Bronkalla, O., & Morschhauser, A. (2021). The geomagnetic Kp index and derived indices of geomagnetic activity. *Space Weather*, *19*(5), e2020SW002641. https://doi.org/10.1029/2020SW002641

NASA. (2023). National Aeronautics and Space Administration Goddard Space Flight Center—OMNI data set [Dataset]. Retrieved from https://omniweb.gsfc.nasa.gov/form/dx1.html

NCEI Geomagnetic Modeling Team, & British Geological Survey. (2019). World magnetic model 2020 [Dataset]. *NOAA National Centers for Environmental Information*. https://doi.org/10.25921/11V3-DA71

NRC. (2023). National Research Council Canada—Solar weather monitoring [Dataset]. Retrieved from https://www.spaceweather.gc.ca/index-en.php

Pesnell, W. D., Thompson, B. J., & Chamberlin, P. C. (2011). The solar dynamics observatory (SDO). *Solar Physics*, *275*(1–2), 3–15. https://doi.org/10.1007/s11207-011-9841-3

Rao, S. S., Sharma, S., Galav, P., & Pandey, R. (2014). Variation of monthly mean foF2 and hmF2 over a mid latitude station during the period 1997–2006. *Advances in Space Research*, *53*(5), 744–751. https://doi.org/10.1016/j.asr.2013.12.018

Ren, D., Lei, J., Wang, W., Burns, A., Luan, X., & Dou, X. (2018). Does the peak response of the ionospheric F2 region plasma lag the peak of 27-day solar flux variation by multiple days? *Journal of Geophysical Research: Space Physics*, *123*(9), 7906–7916. https://doi.org/10.1029/2018ja025835

Schmölter, E., Berdermann, J., & Codrescu, M. (2021). The delayed ionospheric response to the 27-day solar rotation period analyzed with GOLD and IGS TEC data. *Journal of Geophysical Research: Space Physics*, *126*(2), e2020JA028861. https://doi.org/10.1029/2020ja028861

Schmölter, E., Berdermann, J., Jacobi, C., & Jakowski, N. (2020). Modeling of the delayed ionospheric response with the TIE-GCM model. In *2020 European Navigation Conference (ENC)* (pp. 1–9). IEEE. https://doi.org/10.23919/enc48637.2020.9317355

Schmölter, E., Berdermann, J., Jakowski, N., & Jacobi, C. (2020). Spatial and seasonal effects on the delayed ionospheric response to solar EUV changes. *Annales Geophysicae*, *38*(1), 149–162. https://doi.org/10.5194/angeo-38-149-2020

Schmölter, E., Berdermann, J., Jakowski, N., Jacobi, C., & Vaishnav, R. (2018). Delayed response of the ionosphere to solar EUV variability. *Advances in Radio Science*, *16*, 149–155. https://doi.org/10.5194/ars-16-149-2018

Schmölter, E., Heymann, F., Savigny, C., & Berdermann, J. (2022). The height-dependent delayed ionospheric response to solar EUV. *Journal of Geophysical Research: Space Physics*, *127*(3), e2021JA030118. https://doi.org/10.1029/2021ja030118

Schmölter, E., & von Savigny, C. (2022). Solar activity driven 27-day signatures in ionospheric electron and molecular oxygen densities. *Journal of Geophysical Research: Space Physics*, *127*(9), e2022JA030671. https://doi.org/10.1029/2022ja030671

Sethi, N. K., Dabas, R. S., & Vohra, V. K. (2004). Diurnal and seasonal variations of hmF2 deduced from digitalionosonde over New Delhi and its comparison with IRI 2001. *Annales Geophysicae*, *22*(2), 453–458. https://doi.org/10.5194/angeo-22-453-2004

Tapping, K. F. (2013). The 10.7 cm solar radio flux (F10.7). *Space Weather*, *11*(7), 394–406. https://doi.org/10.1002/swe.20064

Vaishnav, R., Jacobi, C., & Berdermann, J. (2019). Long-term trends in the ionospheric response to solar extreme-ultraviolet variations. *Annales Geophysicae*, *37*(6), 1141–1159. https://doi.org/10.5194/angeo-37-1141-2019

Vaishnav, R., Jacobi, C., Berdermann, J., Codrescu, M., & Schmölter, E. (2021). Role of eddy diffusion in the delayed ionospheric response to solar flux changes. *Annales Geophysicae*, *39*(4), 641–655. https://doi.org/10.5194/angeo-39-641-2021

Vaishnav, R., Jacobi, C., Berdermann, J., Schmölter, E., & Codrescu, M. (2018). Ionospheric response to solar EUV variations: Preliminary results. *Advances in Radio Science*, *16*, 157–165. https://doi.org/10.5194/ars-16-157-2018

Vaishnav, R., Jacobi, C., Berdermann, J., Schmölter, E., Dühnen, H., & Codrescu, M. (2023). Ionospheric response to solar EUV radiation variations using GOLD observations and the CTIPe model. *Journal of Geophysical Research: Space Physics*, *129*(1). https://doi.org/10.1029/2022ja030887

Vaishnav, R., Schmölter, E., Jacobi, C., Berdermann, J., & Codrescu, M. (2021). Ionospheric response to solar extreme ultraviolet radiation variations: Comparison based on CTIPe model simulations and satellite measurements. *Annales Geophysicae*, *39*(2), 341–355. https://doi.org/10.5194/angeo-39-341-2021

Woods, T. N., Eparvier, F. G., Hock, R., Jones, A. R., Woodraska, D., Judge, D., et al. (2010). Extreme ultraviolet variability experiment (EVE) on the solar dynamics observatory (SDO): Overview of science objectives, instrument design, data products, and model developments. *Solar Physics*, *275*(1–2), 115–143. https://doi.org/10.1007/s11207-009-9487-6